Parameterization of Size of Organic and Secondary Inorganic Aerosol for

Efficient Representation of Global Aerosol Optical Properties

Haihui Zhu[1]*, Randall V. Martin[1,2], Betty Croft[2,1], Shixian Zhai[3], Chi Li[1], Liam Bindle[1], Jeffrey R. Pierce[4], Rachel Y.-W. Chang[2], Bruce E. Anderson[5], Luke D. Ziemba[5], Johnathan W. Hair[5], Richard A. Ferrare[5], Chris A. Hostetler[5], Inderjeet Singh[1], Deepangsu Chatterjee[1], Jose L. Jimenez[6], Pedro Campuzano-Jost[6], Benjamin A. Nault[7], Jack E. Dibb[8], Joshua S. Schwarz[9], Andrew Weinheimer[10]

[1] Department of Energy, Environmental & Chemical Engineering, Washington University in St. Louis, St. Louis, MO, USA

[2] Department of Physics and Atmospheric Science, Dalhousie University, Halifax, Nova Scotia, Canada

[3] Harvard John A. Paulson School of Engineering and Applied Sciences, Harvard University, Cambridge, MA, USA

[4] Department of Atmospheric Science, Colorado State University, Fort Collins, CO, USA

[5] NASA Langley Research Center, Hampton, VA, USA

[6] Cooperative Institute for Research in Environmental Sciences and Department of Chemistry, University of Colorado, Boulder, CO, USA

[7] Center for Aerosol and Cloud Chemistry, Aerodyne Research, Inc., Billerica, MA, USA

[8] Institute for the Study of Earth, Oceans, and Space, University of New Hampshire, Durham, NH, USA

[9] National Oceanic and Atmospheric Administration Chemical Sciences Laboratory, Boulder, CO, USA

[10] National Center for Atmospheric Research, Boulder, CO, USA

Correspondence: Haihui Zhu (haihuizhu@wustl.edu)

Abstract Accurate representation of aerosol optical properties is essential for modeling and remote sensing of atmospheric aerosols. Although aerosol optical properties are strongly dependent upon the aerosol size distribution, use of detailed aerosol microphysics schemes in global atmospheric models is inhibited by associated computational demands. Computationally efficient parameterizations for aerosol size are needed. In this study, airborne measurements over the United States (DISCOVER-AQ) and South Korea (KORUS-AQ) are interpreted with a global chemical transport model (GEOS-Chem) to investigate the variation in aerosol size when organic matter (OM) and sulfate-nitrate-ammonium (SNA) are the dominant aerosol components. The airborne measurements exhibit a strong correlation (r = 0.83) between dry aerosol size and the sum of OM and SNA mass concentration (M_{SNAOM}). A global microphysical simulation (GEOS-Chem-TOMAS) indicates that M_{SNAOM}, and the ratio between the two components ($\frac{OM}{SNA}$) are the major indicators for SNA and OM dry aerosol size. A parameterization of dry effective radius (R_{eff}) for SNA and OM aerosol is proposed, which well represents the airborne measurements ($R^2 = 0.74$, slope = 1.00) and the GEOS-Chem-TOMAS simulation ($R^2 = 0.72$, slope = 0.81). When applied in the GEOS-Chem high-performance model, this parameterization improves the agreement between the simulated aerosol optical depth (AOD) and the

34   ground-measured AOD from the Aerosol Robotic Network (AERONET; R^2 from 0.68 to 0.73, slope from 0.75 to

35   0.96). Thus, this parameterization offers a computationally efficient method to represent aerosol size dynamically.

1   Introduction

37   Aerosol size has numerous effects on aerosol physical and chemical properties and further on atmospheric chemistry.

38   Aerosol size-dependent heterogeneous chemistry affects gaseous oxidants that in turn affect production rates of

39   aerosol components such as sulfate and secondary organic aerosol (Ervens et al., 2011; Estillore et al., 2016). Aerosol

40   size also affects loss rates due to dry and wet deposition (Seinfeld & Pandis, 2016). Both direct and indirect aerosol

41   radiative forcing are sensitive to aerosol size due to the strong size dependence of aerosol extinction and of the number

42   of cloud condensation nuclei (Adams & Seinfeld, 2002; Emerson et al., 2020; Faxvog & Roessler, 1978; Mishchenko

43   et al., 2002). The size dependence of aerosol extinction and scattering phase function also affects the retrieval of

44   aerosol properties from satellites (Jin et al., 2022; Kahn et al., 2005; Levy et al., 2013). Aerosol size affects the fraction

45   of particles that deposit in the body when breathing as well as location within the body where they deposit (Hinds &

46   Zhu, 1999). An appropriate representation of aerosol size is essential for modeling aerosol composition and optical

47   properties (Kodros & Pierce, 2017), interpreting satellite data (Kahn et al., 2005; Levy et al., 2013), studying climate

48   processes (Kellogg, 1980; Twomey, 2007), and moving from aerosol exposure towards dose in health studies (Kodros

49   et al., 2018).

50   The evolution of the aerosol size distribution is affected by various processes, such as nucleation, condensation,

51   coagulation, and deposition. Nucleation events contribute to the number of particles in the nucleation mode (diameters

52   less than about 10 nm) and thus tend to decrease the mean aerosol size for a population (Aalto et al., 2001). In polluted

53   areas with high emission rates of aerosol precursors, mean aerosol size tends to increase by condensation and

54   coagulation (Sakamoto et al., 2016; Sun et al., 2011). Dry and wet aerosol deposition have strong size dependencies

55   due to competing physical processes (Emerson et al., 2020; Reutter et al., 2009; Ruijrok et al., 1995). The aerosol size

56   distribution can be simulated using aerosol microphysical schemes, such as the TwO Moment Aerosol Sectional

57   (TOMAS; Adams & Seinfeld, 2002) microphysics model, the Advanced Particle Microphysics (APM; Yu & Luo,

58   2009) model, the Global Model of Aerosol Processes (GLOMAP; Mann et al., 2010), and the Modal Aerosol Module

59   (MAM4; X. Liu et al., 2016). These schemes have valuable prognostic capabilities; however, their computational cost

60   has limited their use in Chemistry Climate Models (CCMs) or Chemical Transport Models (CTMs). For example,

61   only 3 of the 10 models that included aerosols, studied by the Atmospheric Chemistry and Climate Model

62   Intercomparison Project, include online size-resolved aerosol microphysics (Kodros & Pierce, 2017; Lamarque et al.,

63   2013).

64   Methods are needed to better represent aerosol size in CCMs or CTMs without a microphysics scheme (referred to as

65   bulk models). These bulk models usually use prescribed relationships to obtain size-resolved aerosol properties (Croft

66   et al., 2005; Karydis et al., 2011; Zhai et al., 2021), which may insufficiently represent the temporal and spatial

67   variation (Kodros & Pierce, 2017). For example, in the GEOS-Chem CTM, a fixed dry aerosol geometric mean radius

68   (R_g) is assumed for organic matter (OM) and sulfate-nitrate-ammonium (SNA), which is based on analysis of long-

69   term aerosol composition and scattering measurements provided by the IMPROVE network across the continental

70   U.S. (Latimer & Martin, 2019). However, subsequent analysis by Zhai *et al.* (2021) found that this aerosol size

71   underestimated the aerosol mass scattering efficiency and the aerosol extinction coefficients during an aircraft

72   campaign over South Korea (KORUS-AQ). Thus, neglect of aerosol microphysical processes that shape aerosol size

73   distributions can be a significant source of uncertainty in aerosol optical properties in a CTM. A balance between

74   computational cost and representativeness of aerosol size is needed. One option is to use models with size-resolved

75   aerosol microphysics models to inform bulk models, such as was done for the parameterization of biomass burning

76   aerosol size by Sakamoto *et al*. (2016).

77   Recent airborne measurements offer information to evaluate and improve the simulation of aerosol size. DISCOVER-

78   AQ (Deriving Information on Surface Conditions from Column and Vertically Resolved Observations Relevant to Air

79   Quality) was a multi-year campaign over four U.S. cities that provides 3-D resolved measurements of atmospheric

80   gas composition, aerosol composition, size distribution, and optical properties (Choi et al., 2020; Chu et al., 2015;

81   Sawamura et al., 2017). KORUS-AQ (the Korea-United States Air Quality Study) offers similar measurements in a

82   different environment with higher aerosol mass loadings (Choi et al., 2020; Jordan et al., 2020; Nault et al., 2018; Zhai

83   et al., 2021).

84   To study the global variation in aerosol size, we explore airborne measurements from DISCOVER-AQ and KORUS-

85   AQ, as well as output from the GEOS-Chem-TOMAS microphysics model. We focus on OM and SNA, which

86   dominate fine aerosol composition in populated areas. The driving factors for variation in aerosol size are examined.

87   A parameterization of aerosol size using these driving factors is proposed. This parameterization is then applied to a

88   GEOS-Chem high-performance model bulk simulation for global aerosol optical depth (AOD), which is evaluated by

89   ground-measured AOD from the Aerosol Robotic Network (AERONET).

90   **2   Observations and Models**

91   **2.1   Observations**

92   **2.1.1   Aircraft measurements**

93   We examine airborne measurements from two NASA campaigns, DISCOVER-AQ and KORUS-AQ. DISCOVER-

94   AQ includes four deployments in Maryland (MD), California (CA), Texas (TX), and Colorado (CO). KORUS-AQ is

95   an international cooperative field study program conducted in South Korea (KO), sponsored by NASA and the South

96   Korean government through the National Institute of Environmental Research. The year as well as the date and altitude

97   ranges of each deployment are in Table 1.

98   **Table 1. Temporal and spatial coverage of each aircraft deployment**

Campaign	Year	Date Range	Altitude from surface
MD	2011	07/01-07/29	0 to 5 km
TX	2013	09/04-09/29	0 to 5 km

CA	2013	01/16-02/06	0 to 4 km
CO	2014	07/17-08/10	0 to 6 km
KO	2016	05/02-06/11	0 to 8 km

99

100 Measurements used in this study include aerosol composition, ambient aerosol extinction coefficients, aerosol number
101 size distribution, gas tracer species, and meteorological data. Measurement methods are listed in Table 2. Measured
102 aerosol mass is converted from standard to ambient condition before analysis using ambient temperature and pressure.
103 We use OM directly measured during KORUS-AQ. We use water soluble organic carbon (OC) and a parameterized
104 ratio between OM and OC (Philip et al., 2014) to calculate OM for DISCOVER-AQ. The parameterized OM is
105 evaluated with KORUS-AQ data, and overall consistency is found (Figure A1; Appendix A). For both campaigns,
106 dust concentration is derived from Ca^{2+} and Na^+ assuming non-sea salt Ca^{2+} accounts for 7.1% of dust mass (Shah et
107 al., 2020):

$$Dust = \frac{\left([Ca^{2+}] - 0.0439\frac{[Na^+]}{2}\right)}{0.071} \qquad \text{Eqn. (1)}$$

108 Sea salt is calculated from measured Na^+ following previous studies (Malm et al., 1994; Remoundaki et al., 2013;
109 Snider et al., 2016). The crustal component is removed by subtracting 10 % of $[Al^{3+}]$ (Remoundaki et al., 2013). A
110 2.54 scalar is applied to $[Na^+]_{ss}$ to account for $[Cl^-]$ (Malm et al., 1994):

$$Sea\ Salt = 2.54([Na^+] - 0.1[Al^{3+}]) \qquad \text{Eqn. (2)}$$

111 Effective radius (R_{eff}; Hansen & Travis, 1974), defined as the area-weighted mean radius of a particle population, is
112 used as a surrogate for aerosol size:

$$R_{eff} = \frac{\int r\pi r^2 n(r)dr}{\int \pi r^2 n(r)dr} \qquad \text{Eqn. (3)}$$

113 Measurement data are screened for dust influence by excluding data with the sum of SNA and OM (M_{SNAOM}) < 4 ×
114 dust mass.

115 **Table 2. Aircraft observations used in this study[*]**

Variables	DISCOVER-AQ	KORUS-AQ
Bulk aerosol ionic composition	IC-PILS [a]	SAGA [b]
Sub-micron non-refractory aerosol composition	TOC-PILS [c]	HR-ToF-AMS [d]
Refractory black carbon concentration	SP2 [e]	
Dry aerosol size distribution	UHSAS [f] or LAS [g]	LAS [g]

Aerosol extinction profile at 532 nm	HSRL [h]
NO$_2$	4-Channel Chemiluminescence Instrument [i]
Relative humidity (RH)	DLH [j]

116   [*] Adapted from Zhai et al. (2021)

117   [a] Ion Chromatography Particle-Into-Liquid Sampler, with a 1.3 µm inlet cutoff aerodynamic diameter
118   (Hayes et al., 2013; Lee et al., 2003).

119   [b] Soluble Acidic Gases and Aerosol (SAGA) instrument (Dibb et al., 2003). The cutoff aerodynamic
120   diameter of the inlet is around 4 µm (McNaughton et al., 2007).

121   [c] Water-soluble organic carbon Particle-Into-Liquid Sampler, with a 1 µm inlet cutoff diameter at 1
122   atmosphere ambient pressure (Sullivan et al., 2019; Timonen et al., 2010).

123   [d] University of Colorado Boulder High-Resolution Time-of-Flight Aerosol Mass Spectrometer (HR-ToF-
124   AMS) with a 1 µm inlet cutoff diameter (Canagaratna et al., 2007; Guo et al., 2021; Nault et al., 2018).

125   [e] Single-Particle Soot Photometer (SP2), measuring refractory black carbon with a volume equivalent
126   diameter of 100-500 nm (Lamb et al., 2018; Schwarz et al., 2006).

127   [f] Particles with mobility diameters between 60 to 1000 nm can be measured by Ultra-High Sensitivity
128   Aerosol Spectrometer (UHSAS), which illuminates particles with a laser and relate the single-particle light
129   scattering intensity and count rate measured over a wide range of angles to the size-dependent particle
130   concentration (Moore et al., 2021). Particles in the sample are dried to less than 20 % RH.

131   [g] Particles between 100 to 5000 nm measured by Laser Aerosol Spectrometer (LAS, TSI model 3340). The
132   principle of LAS is the same as that of UHSAS, but with a different laser wavelength (1054 nm for the
133   UHSAS and 633 nm for the LAS) and intensity (about 100 times higher for the UHSAS). These differences
134   affect how the instrument sizes non-spherical or absorbing aerosols (Moore et al., 2021). Particles in the
135   sample are dried to less than 20 % RH.

136   [h] NASA Langley airborne High Spectral Resolution Lidar (HSRL; Hair et al., 2008).

137   [i] National Center for Atmospheric Research (NCAR) 4-Channel Chemiluminescence Instrument
138   (Weinheimer et al., 1993)

139   [j] NASA Diode Laser Hygrometer (DLH; Podolske et al., 2003).

2.1.2   AERONET AOD

We use ground-based AOD observations to evaluate our parameterization and simulated AOD. Aerosol Robotic Network (AERONET) is a worldwide network that provides long-term sun photometer measured AOD. We use the Version 3 Level 2 database, which includes an improved cloud screening algorithm (Giles et al., 2019). AOD at 550 nm wavelength, interpolated based on the local Ångström exponent at 440 and 670 nm channels, is used in this study. For each site, we use data for the year 2017, excluding months with less than 20 days of measurements and excluding sites with data less than 4 months.

2.2   GEOS-Chem simulation

We interpret the aircraft observations with the GEOS-Chem chemical transport model (www.geos-chem.org, last access: 30 October 2022). GEOS-Chem is driven by offline meteorological data from the Goddard Earth Observing System (GEOS) of the NASA Global Modeling and Assimilation Office (Schubert et al., 1993). We use the high-performance implementation of GEOS-Chem (GCHP; Eastham et al. 2018) to examine the effect of variation in aerosol size on AOD. We also use the TOMAS microphysical scheme, coupled with the standard GEOS-Chem implementation (GEOS-Chem classic), to explicitly resolve aerosol microphysics. The bulk and the microphysics simulations share common emissions and chemical mechanisms. They are both conducted for the year 2017 and driven by MERRA-2 meteorological fields.

The GEOS-Chem aerosol simulation includes the sulfate-nitrate-ammonium system (Fountoukis & Nenes, 2007; Park, et al., 2004), primary and secondary carbonaceous aerosols (Marais et al., 2016; Park et al., 2003; Pye et al., 2010; Wang et al., 2014), sea salt (Jaeglé et al., 2011), and mineral dust (Fairlie et al., 2007). The primary emission data are from the Community Emissions Data System (CEDS$_{GBD-MAPS}$; McDuffie et al. 2020). Dust emission inventories include updated natural dust emission (Meng et al., 2021), and anthropogenic fugitive, combustion, and industrial dust (AFCID; Philip et al., 2017). Resolution-dependent soil NO$_x$, sea salt, biogenic VOC, and natural dust emissions are calculated offline at native meteorological resolution to produce consistent emissions across resolution (Meng et al., 2021; Weng et al., 2020). Biomass burning emissions use the Global Fire Emissions Database, version 4 (GFED4) (Van Der Werf et al., 2017). We estimate organic matter (OM) from primary organic carbon using the same OM/OC parameterizations as applied for DISCOVER-AQ (Canagaratna et al., 2015; Philip et al., 2014). Dry and wet deposition follows Amos *et al.* (2012), with a standard resistance-in-series dry deposition scheme (Wang et al., 1998). Wet deposition includes scavenging processes from convection and large-scale precipitation (Liu et al., 2001).

Global relative humidity dependent aerosol optical properties are based on the Global Aerosol Data Set (GADS; Koepke et al. 1997; Martin et al. 2003) with updates for SNA and OM (Latimer & Martin, 2019), mineral dust (Zhang et al., 2013), and absorbing brown carbon (Hammer et al., 2016). In the current GEOS-Chem model, the SNA and OM R$_{eff}$ of particular interest here are based on co-located measurements of aerosol scatter and mass from the IMPROVE network at U.S. national parks over the period 2000-2010, together with a κ-Kohler framework for aerosol hygroscopicity (Kreidenweis et al., 2008) as implemented by Latimer and Martin (2019). Aerosol extinction is

174   calculated as the sum of extinction from each aerosol component with aerosol optical properties listed in Table A1, as

175   described in Appendix A2.

176   A global GCHP simulation (Eastham et al. 2018) version 13.0.0 (DOI: 10.5281/zenodo.4618180) that includes

177   advances in performance and usability (Martin et al., 2022), is conducted on a C90 cubed-sphere grid corresponding

178   to a horizontal resolution of about 100 km.

179   The TOMAS microphysics scheme, coupled with the GEOS-Chem simulation, conserves aerosol mass, and tracks

180   particles with diameters from approximately 1 nm to 10 μm (Adams & Seinfeld, 2002). Microphysical processes in

181   TOMAS include nucleation, condensation, evaporation, coagulation, and wet and dry deposition (Adams & Seinfeld,

182   2002). Nucleation in TOMAS follows a ternary scheme (sulfuric acid, ammonia, and water) when ammonia mixing

183   ratios are greater than 0.1 ppt; otherwise, a binary nucleation scheme is used (Napari et al., 2002). The nucleation rate

184   is scaled by 10^{-5} to better match the observations (Westervelt et al., 2013). The condensation and evaporation algorithm

185   is based on a study from Tzivion *et al.* (1989), including interaction with secondary organic aerosol (D'Andrea et al.,

186   2013). Interstitial coagulation in clouds is also included (Pierce et al., 2015).

187   For each size bin, TOMAS tracks the mass and number of sulfate, sea salt, black carbon, OC, dust, and water. Primary

188   sulfate emissions have 2 lognormal modes: 15% of the mass with a number median diameter (NMD) of 10 nm and

189   geometric standard deviation (σ) of 1.6 and the remainder with a NMD of 70 nm and σ of 2 (Adams & Seinfeld, 2003).

190   The size of emitted carbonaceous particles varies depending on the source: those produced by fossil fuel have a NMD

191   of 30 nm and σ of 2, while biofuel and biomass burning particles are emitted with a NMD of 100 nm and σ of 2 (Pierce

192   et al., 2007). Meteorology and most of the emissions in GEOS-Chem-TOMAS follow the bulk simulation, except that

193   online schemes are used for dust (Zender et al., 2003) and sea salt (Jaeglé *et al.* 2011).

194   A one-year global GEOS-Chem-TOMAS (version 13.2.1. DOI: 10.5281/zenodo.5500717) simulation is conducted

195   with a horizontal resolution of 4º × 5º and 47 vertical layers from surface to 0.01 hPa. Aerosols are tracked in 15 size

196   bins with particle diameters ranging from about 3 nm to 10 μm.

197   **3   Development of a Parameterization of Aerosol Size**

198   We first examine the aircraft measurements for insight into the observed variation in aerosol size. Then we apply the

199   size-resolved GEOS-Chem-TOMAS model to extend our analysis to the global scale and identify driving factors of

200   aerosol size. We subsequently develop and test a parameterization of aerosol size for use in bulk models.

201   **3.1   Observed variation in aerosol size**

202   Figure 1 shows the daily-mean dry effective radius from DISCOVER-AQ and KORUS-AQ as a function of aerosol

203   mass. Aerosol size, in terms of dry R_{eff}, ranges from 90 nm to 179 nm for DISCOVER-AQ, which is generally smaller

204   than for KORUS-AQ that ranges from 135 nm to 174 nm. M_{SNAOM} from DISCOVER-AQ (1.4 μg/m³ to 27.4 μg/m³)

205   is also generally less than that from KORUS-AQ (5.5 μg/m³ to 33.2μg/m³). A strong correlation (r = 0.83) between

206   aerosol size and M_{SNAOM} is evident.

207
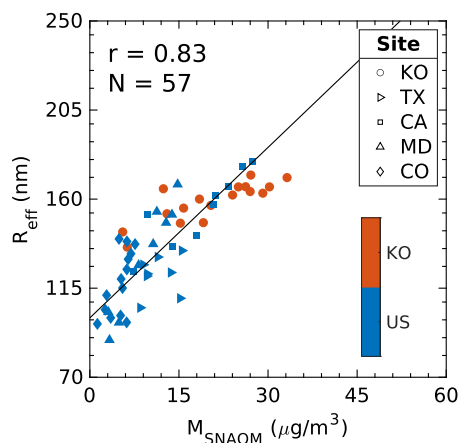
Figure 1. Airborne measurements of dry effective radius (R_{eff}) versus the sum of SNA and OM mass

(M_{SNAOM}) for DISCOVER-AQ (Maryland is abbreviated as MD, California as CA, Texas as TX, Colorado as

CO) and for KORUS-AQ (KO) campaigns. Each point represents a daily average for the entire flight profile.

Only data with $M_{SNAOM} > 4 \times$ Dust mass is used.

The positive relationship between dry aerosol size and mass of SNA and OM reflects the roles of emission, condensation, and coagulation in simultaneously increasing aerosol size and mass. This general tendency is also observed by many other studies (e.g., Bahreini et al., 2003; Rodríguez et al., 2007; Sakamoto et al., 2016; Sun et al., 2010) despite variable aerosol sources and growth mechanisms. In cities, the joint increases in aerosol size and mass are usually attributable to anthropogenic emissions and condensation (Huang et al., 2013; Sun et al., 2011; Tian et al., 2019). In remote areas, biomass burning shifts the particle size distribution toward larger radii due to high emission rates and coagulation in plumes (Ramnarine et al., 2019; Rissler et al., 2006) that, for example, increase both aerosol size and mass from the wet season to the dry season in Amazonia (Andreae et al., 2015; Rissler et al., 2006). The positive relationship between aerosol size and mass suggests the possibility of using aerosol mass as a predictor of R_{eff}.

We examine the ability of the GEOS-Chem bulk model to reproduce the observed extinction. The top panel of Figure 2 compares the measured aerosol extinction profiles to calculated aerosol extinction profiles using default R_{eff}. Details about the calculation are described in Appendix A2. Both measured and calculated extinction profiles exhibit increasing extinction toward the surface associated with increasing aerosol mass concentrations. However, biases are apparent for both DISCOVER-AQ and KORUS-AQ. The R_{eff} from KORUS-AQ shown in Figure 1 have a mean value of 164 nm, larger than the value of 101 nm inferred by Latimer & Martin (2019) based on measurements of aerosol scatter and mass by the U.S. IMPROVE network. This bias was previously noted by Zhai *et al.* (2021). The mean R_{eff} from DISCOVER-AQ of 138 nm is also larger than the inferred value. This likely reflects representativeness differences since the DISCOVER-AQ deployments focused on major urban areas during months of high aerosol loadings, while the IMPROVE measurements were at national parks throughout the year. The middle panel shows the

232 calculated extinction using the measured aerosol size distribution. Applying the measured aerosol size distribution

233 addresses most discrepancies between the calculated and measured aerosol extinction profile for both KORUS-AQ

234 and DISCOVER-AQ. The corresponding discrepancies in AOD estimation also significantly decreased (from 0.09 to

235 0.03 for DISCOVER-AQ and from 0.17 to 0.02 for KORUS-AQ). The reduced discrepancies support the conclusions

236 from Zhai *et al.* (2021) that the GEOS-Chem aerosol size is underestimated for KORUS-AQ and motivate

237 parameterization of R_{eff} for efficient representation of aerosol size for global scale aerosol modeling.
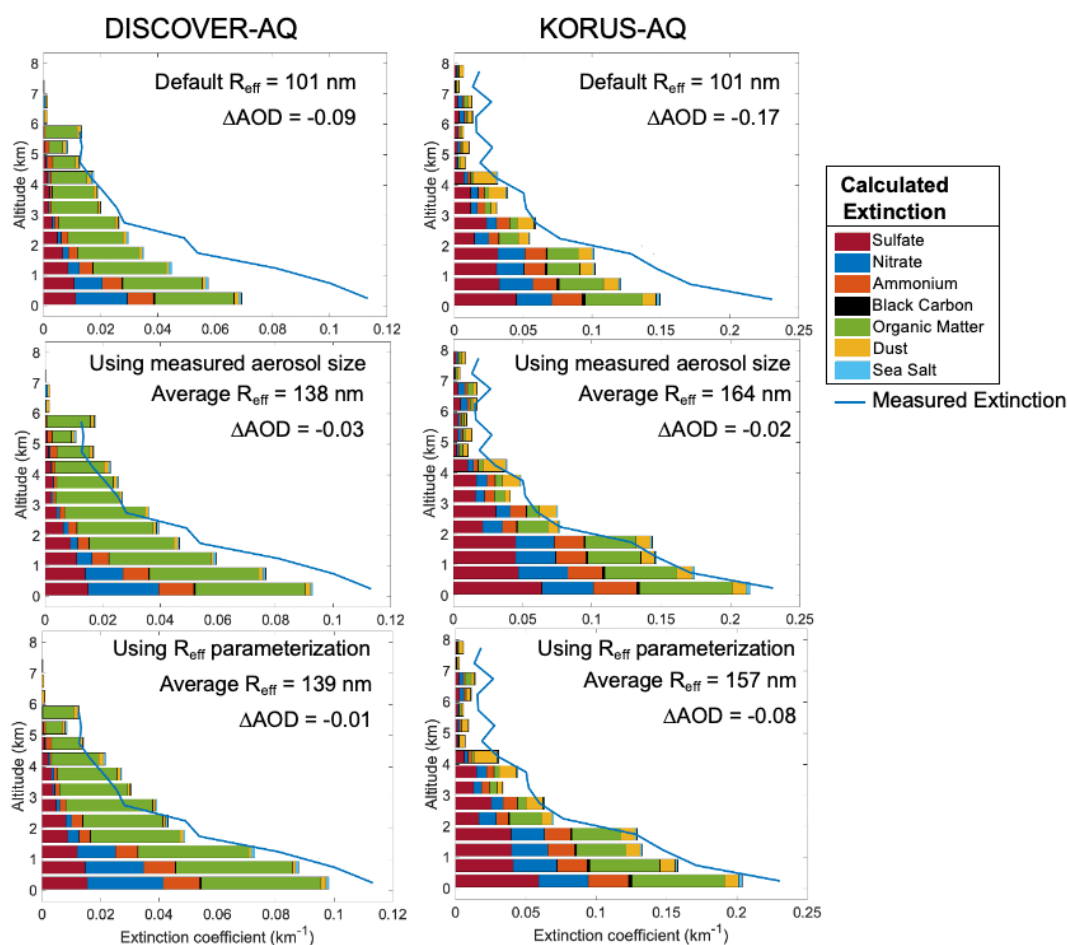
238

239 **Figure 2. Aerosol extinction profile for the DISCOVER-AQ and KORUS-AQ aircraft campaigns. Blue lines**

240 **are the measured extinction profiles. Horizontal bars are calculated extinction using (top) default GEOS-**

241 **Chem R_{eff}, (middle) measured R_{eff}, and (bottom) parameterized R_{eff} (described in Section 3.3), together with**

242 **measured aerosol composition and RH. The aerosol extinction calculation is described in Appendix A.**

3.2   Driving factors

Given the strong positive correlation of aerosol mass with aerosol size, we further examine this relationship globally using GEOS-Chem coupled with the TOMAS aerosol microphysics scheme. The top panel of Figure 3 shows the geographic distribution of annual mean surface layer dry R_{eff} for locations and months where aerosol mass is dominated by SNA and OM, as indicated by M_{SNAOM} > 90% of the aerosol mass. Among the areas of interest, biomass burning regions of Central Africa, South America, and boreal forest of North America exhibit the highest surface R_{eff} of about 180 nm. Industrial areas such as East Asia and South Asia also exhibit high R_{eff} of about 130 nm, given an abundance of particle emissions and gaseous precursors. The lowest surface R_{eff} of about 80 nm is found in North America, where aerosol mass concentrations are low.

The middle panel of Figure 3 shows the simulated M_{SNAOM} from GEOS-Chem-TOMAS. Enhanced M_{SNAOM} concentrations of over 40 μg/m^3 are apparent over East Asia and South Asia, reflecting intense anthropogenic emissions. Another M_{SNAOM} hotspot can be seen in Central Africa, driven by biomass burning during the dry season (McDuffie et al., 2021; Van Der Werf et al., 2017) and sometimes exacerbated by anthropogenic emissions (Ngo et al., 2019). Moving from North America, to Europe, and then to Asia, M_{SNAOM} concentrations exhibit a generally increasing tendency, consistent with the R_{eff} tendency in the top panel and aligning with the relationship between aircraft measurements over the U.S. and South Korea.

However, in South America, where R_{eff} is among the highest, M_{SNAOM} is relatively low. This discrepancy motivates the search for other factors, such as aerosol composition, that are associated with aerosol size. In South America, aerosol mass is mostly from natural sources, particularly biomass burning during the dry seasons. R_g for a particle population from biomass burning ranges from 60 nm to 170 nm (Janhäll et al., 2010; Reid et al., 2005; Rissler et al., 2006), usually larger than that of primary sulfate aerosol (5 to 35 nm; Plaza et al., 2011; Whitey, 1978). Therefore, the relative abundance of OM in the total M_{SNAOM} can serve as another predictor of R_{eff}. The bottom panel of Figure 3 shows the ratio between OM and SNA mass. In addition to the Amazon basin, the biomass burning regions of Central Africa and boreal forests in Asia and North America are all areas with high OM mass fractions, which contribute to their high R_{eff} despite the low M_{SNAOM}.

268
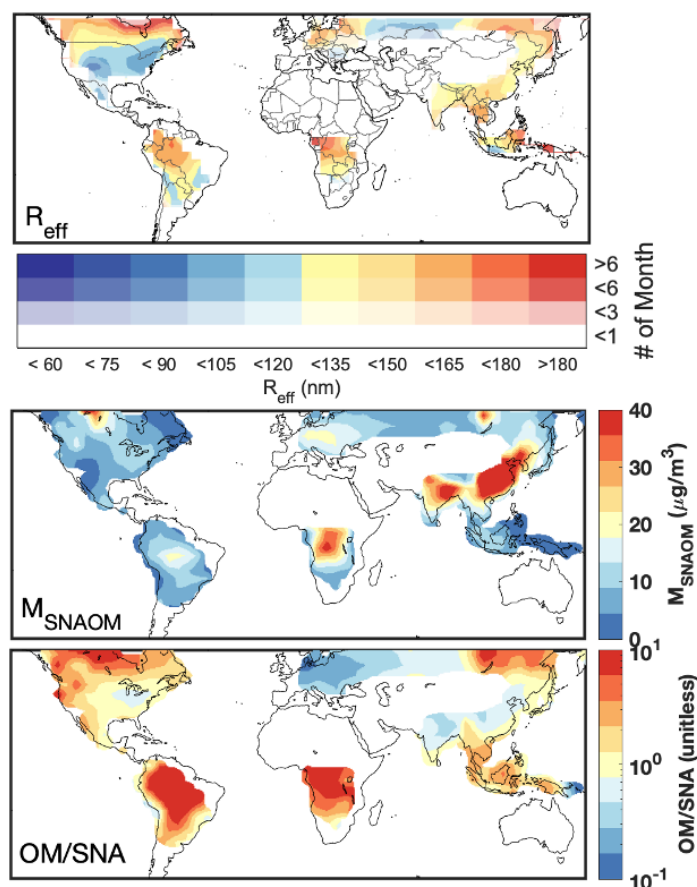
Figure 3: Geographic distribution of GEOS-Chem-TOMAS-simulated annual mean surface layer aerosol properties; (top) R_{eff} with color intensity indicating the number of months included (Mass of SNA and OM > 90% of aerosol mass), (middle) the sum of SNA and OM mass (M_{SNAOM}), and (bottom) OM/SNA.

272   **3.3   Parameterization and evaluation**

273   We use Multiple Linear Regression (MLR) to derive a parameterization of dry R_{eff} as a function of M_{SNAOM} and

274   OM/SNA. We sample the GEOS-Chem-TOMAS simulation for locations dominated by M_{SNAOM} (> 90%). We include

275   all qualified data (8,569 grid boxes) from the planetary boundary layer (PBL) to focus on this region, while randomly

276   sample 0.5% of simulations in the free troposphere (217,772 grid boxes) to allow the influence of remote regions in

277   the training set. The reason for focusing on the PBL is twofold. First, the PBL generally has the highest aerosol loading

278   that largely determines the columnar mass and AOD (Koffi et al., 2016; Tian et al., 2019; Zhai et al., 2021). Second,

279   the PBL is the domain where the model-measurement difference exists (Figure 2, top panel).

280   Taking the logarithm of R_{eff} and the logarithm of the two predictors facilitates linear relationships for regression,

281   which yields the initial parameterization

$$R_{eff} = 78.3 M_{SNAOM}^{0.20} \left(\frac{OM}{SNA}\right)^{0.065} \qquad \text{Eqn. (4)}$$

282   where R_{eff} has units of nm, M_{SNAOM} has units of μg/m³, and OM/SNA is unitless. The R_{eff} parameterization is driven

283   primarily by the mass of SNA and OM, modulated by the ratio of OM to SNA. This equation well represents the

284   variation of R_{eff} during the aircraft campaigns with an R^2 of 0.74 (Figure B1, top left). The slope below unity (0.90)

285   likely reflects the effect of coarse model resolution, which dilutes the particle or precursor concentration in turn

286   reducing condensation and coagulation growth (AboEl-Fetouh et al., 2022; Ramnarine et al., 2019; Sakamoto et al.,

287   2016). Adjustment to this parameterization to account for these effects and align the slope with the airborne

288   measurements rather than the model results in a final parameterization of

$$R_{eff} = 87.0 M_{SNAOM}^{0.20} \left(\frac{OM}{SNA}\right)^{0.065} \qquad \text{Eqn. (5)}$$

289   Figure 4 shows the distribution of dry R_{eff} based on GEOS-Chem-TOMAS and Eqn. (5). Circles in Figure 4 show the

290   mean values of the sampled GEOS-Chem-TOMAS simulated R_{eff} as a function of simulated M_{SNAOM} concentrations,

291   ranging from 0.02 to 102 μg/m³, and OM/SNA ranging from 0.13 to 55. Simulated R_{eff} extends from 15 nm when both

292   M_{SNAOM} and OM/SNA are low (0.09 μg/m³ and 1.3, respectively), up to 282 nm when M_{SNAOM} and OM/SNA are high

293   (about 44 μg/m³ and 14 respectively). The background color indicates our parameterized R_{eff}. A high degree of

294   consistency exists between the parameterized R_{eff} and simulated R_{eff}, especially in the free troposphere where large

295   gradients in R_{eff} exist, with overall for the troposphere an R^2 of 0.72, and a slope of 0.81 (Figure B1, bottom right).

296   Despite the overall consistency, a few differences exist. When aerosol mass concentration is high, the parameterization

297   tends to yield a higher R_{eff} than in the GEOS-Chem-TOMAS simulation, since the adjustment using aircraft

298   measurements led to 11% increase in R_{eff}. At M_{SNAOM} near 10 μg/m³ and OM/SNA near 10, the simulation indicates

299   higher R_{eff} than the parameterization, reflecting dilution downwind of biomass burning that reduces the aerosol mass

300   concentration but has little influence on particle size in GEOS-Chem-TOMAS. A 10-20% underestimation in the

301   parameterization at low OM/SNA reflects the advection and dilution of downwind of urban areas and in the free

302   troposphere.
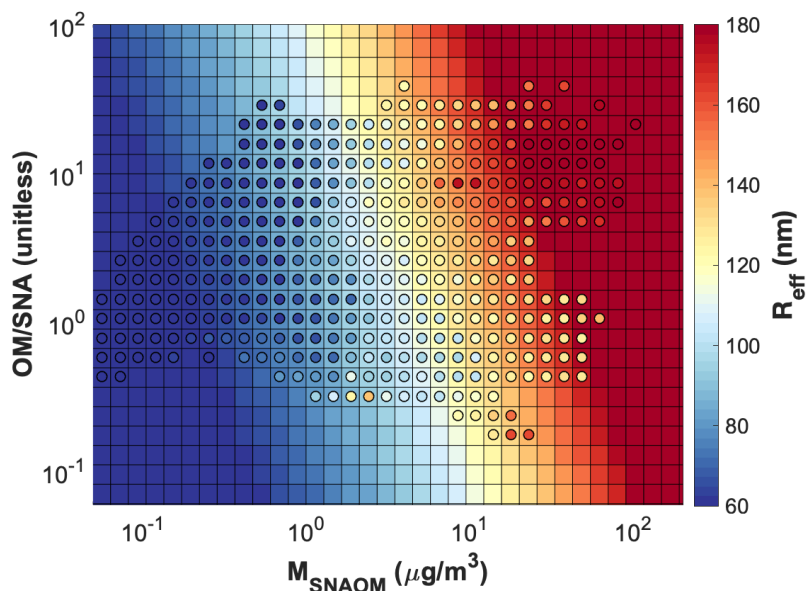
Figure 4. Dry R_{eff} as a function of M_{SNAOM} and OM/SNA when SNA and OM are dominant (>90%). Each circle represents the mean value of the GEOS-Chem-TOMAS simulated R_{eff} in each bin. Background color indicates the parameterized R_{eff}.

When applied to the airborne measurements, this parameterization only slightly overestimates the measured R_{eff} from DISCOVER-AQ (139 nm vs. 138 nm) and slightly underestimates R_{eff} from KORUS-AQ (157 nm vs. 164 nm). Most discrepancies between calculated and measured extinction from aircraft campaigns are eliminated (Figure 2, bottom panel) with AOD discrepancies reduced to 0.01 and 0.08 for DISCOVER-AQ and KORUS-AQ, respectively.

We then apply Eqn. (5) to a GEOS-Chem bulk simulation to calculate R_{eff} and AOD. The top panel of Figure 5 shows the annual mean dry R_{eff} for surface SNA and OM aerosol with the color intensity indicating the ratio of SNA and OM mass to total aerosol mass at the surface. The parameterized R_{eff} is usually higher than the default value of about 100 nm in GEOS-Chem over land, and lower than that over the ocean, with a normalized root mean square deviation (NRMSD) of 43.8%. The spatial pattern well represents the GEOS-Chem-TOMAS simulation, with high R_{eff} found in biomass burning regions in South America and Central Africa, as well as industrial regions in Asia. The horizontal variation diminishes with altitude (Figure B2), with the mean R_{eff} decreasing from 85 nm (surface) to 43 nm (10 km).

The middle panel of Figure 5 shows the simulated AOD, with the corresponding difference between the base simulation and the updated simulation in the bottom panel. To accommodate the parameterized R_{eff}, a look-up table with a wide range of R_{eff} (0.02 µm to 1.7 µm) and the corresponding extinction efficiencies for OM and SNA is created based on Mie Theory (Mishchenko et al., 1999, 2002). This update generally increases aerosol mass scattering by increasing the mass extinction efficiency, in turn, increasing AOD over regions with strong anthropogenic sources,

323   such as East Asia (by 0.13, 35.4%) and South Asia (by 0.13, 28.3%). It also slightly increases AOD over regions

324   influenced by wildfires, such as South America (by 0.02, 12.2%), Central Africa (by 0.03, 17.4%), and the boreal

325   forests in North America, Europe, and Asia (by 0.01-0.03, 12.1 to 16.9%). Most increases occur near the surface

326   (Figure B3), where the highest aerosol mass loading and mass extinction efficiency exist. The NRMSD between

327   original and updated GEOS-Chem simulated AOD is 20.9% globally, and 28.8% over continents.
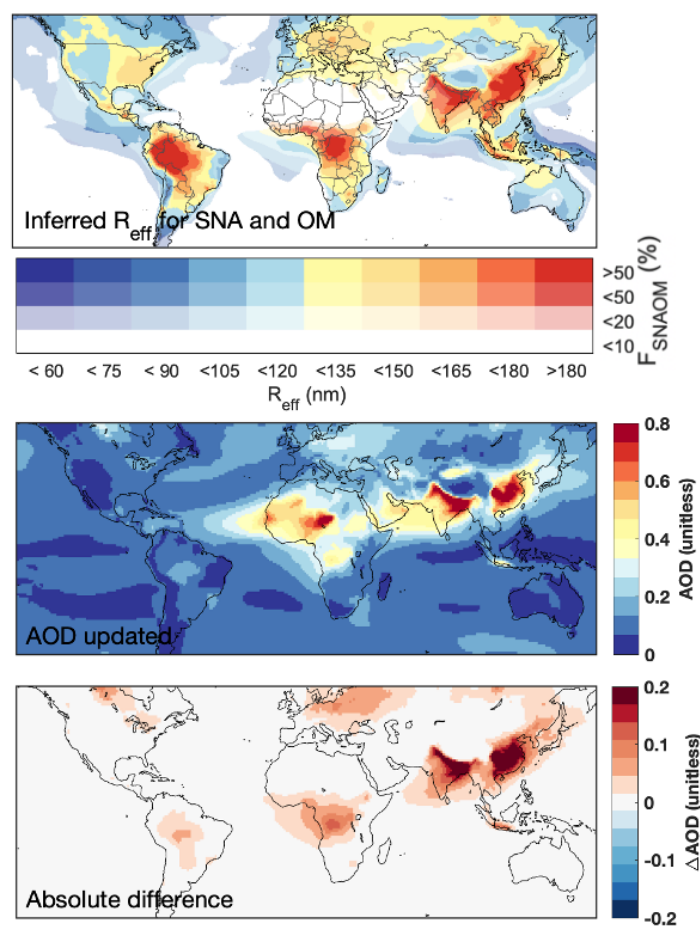
328

329   **Figure 5. (Top) Surface dry R_{eff} for SNA and OM calculated using Eqn. (5) and GEOS-Chem bulk model**

330   **simulated SNA and OM mass. F_{SNAOM} is the ratio of SNA and OM mass to the total aerosol mass at the**

331   **surface. (Middle) The GEOS-Chem simulated AOD using inferred R_{eff}. (Bottom) the absolute difference**

332   **between updated AOD and default AOD using dry $R_{eff} = 101$ nm.**

333   Although R_{eff} is only one of many processes affecting AOD, we evaluate the effect of the parameterization on the

334   GEOS-Chem simulation of AOD to assess its implications. The left panel of Figure 6 shows for the default R_{eff}, the

335 percent difference between GEOS-Chem simulated AOD and AERONET AOD as a function of the parameterized
336 surface R_{eff} for SNA and OM. The simulation using the default R_{eff} slightly overestimates AOD in regions with small
337 parameterized R_{eff} and underestimates AOD in regions with large parameterized R_{eff}. The overestimates occur
338 primarily in western Europe where SNA and OM concentrations are low, while the underestimates happen mainly
339 over industrial regions in East Asia, Southeast Asia, and biomass burning areas in South America and Central Africa,
340 where the SNA and OM mass loading are high (Figure B4). The underestimates are mitigated when applying the
341 parameterized R_{eff} in GEOS-Chem (Figure 6 , middle panel), yielding increased consistency between the measured
342 (AERONET) AOD and simulated AOD (Figure 6, right; R^2 change from 0.68 to 0.73, slope from 0.75 to 0.96).
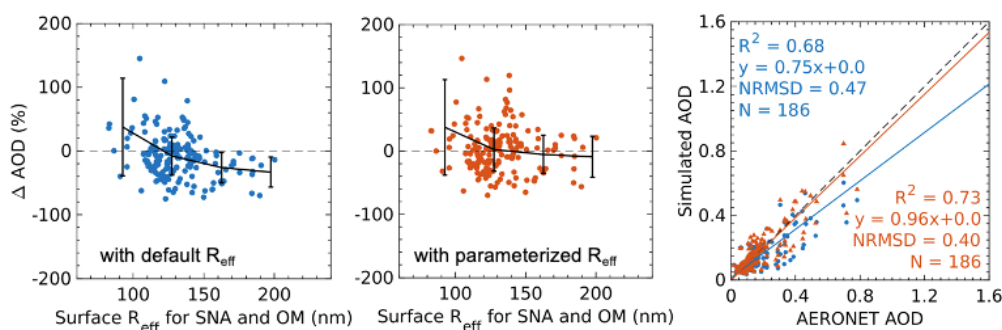
343

344 **Figure 6. (Left and middle) Percent increase in GEOS-Chem simulated AOD minus AERONET AOD as a**
345 **function of parameterized surface dry R_{eff} for SNA and OM. Black lines represent the mean values of ΔAOD**
346 **in each 35 nm bin; error bars represent the corresponding standard deviation. (Right) Scatter plot of**
347 **AERONET versus simulated AOD with the default R_{eff} (blue dots, line, and text), and with the parameterized**
348 **R_{eff} (red dots, line, and text). The 1:1 line is dashed. NRMSD is the normalized root mean square deviation**
349 **between the two datasets. N is the number of points in each dataset.**

350 **4   Conclusion**

351 Aerosol size strongly determines mass scattering efficiency with implications for calculation of aerosol optical
352 properties. Prior work found that the global mean dry aerosol size used in a bulk aerosol model induced low bias
353 versus measured extinction in a region with a high aerosol loading (Zhai et al., 2021). We interpreted aircraft
354 measurements from DISCOVER-AQ and KORUS-AQ with a chemical transport model (GEOS-Chem) to better
355 understand regional variation in aerosol size. The measurements had a strong positive correlation (r = 0.83) between
356 aerosol size and mass of sulfate-nitrate-ammonium (SNA) and organic matter (OM), reflecting the high condensation
357 and coagulation rates where emissions of particles and the gaseous precursors are abundant, indicating the possibility
358 of using aerosol mass as a predictor of aerosol size.

359 To gain a broader perspective of the global variation in aerosol size, we used the TOMAS microphysics package of
360 the GEOS-Chem model to simulate the monthly mean aerosol mass, composition, and size distribution. We used
361 effective radius (R_{eff}) as a surrogate of aerosol size and examined its relationship with aerosol mass and components

362   where SNA and OM were dominant. We found that the sum of SNA and OM concentration, and the ratio between

363   them, were the major predictors of R_{eff}. We used GEOS-Chem-TOMAS model output to derive a parameterization of

364   R_{eff}, which well reproduced R_{eff} measured from the aircraft campaigns ($R^2 = 0.74$). When applied in the bulk GEOS-

365   Chem high-performance model, the parameterization tended to increase R_{eff} of SNA and OM over regions with high

366   concentrations of SNA and OM, and decrease R_{eff} elsewhere relative to the standard model. This led to a global

367   normalized root mean square deviation (NRMSD) of 43.8% between the original and updated surface R_{eff}. The

368   parameterized R_{eff} tended to increase the vertical gradient in extinction relative to the standard model, due to the

369   decrease in R_{eff} with altitude. The NRMSD of global mean AOD between the original and updated simulations was

370   20.9%, with the most significant regional AOD increase of about 0.13 in South and East Asia, where aerosol mass

371   loadings are high. This parameterization led to improved consistency of GEOS-Chem simulated AOD with

372   AERONET AOD (R^2 from 0.68 to 0.73; slope from 0.75 to 0.96), by increasing AOD at high R_{eff}.

373   Overall, the simple parameterization of R_{eff} derived in this study improved the accuracy in modeling aerosol optical

374   properties without imposing additional computational expense. Other chemical transport models and modeling of

375   other size-related processes, such as heterogeneous chemistry, photolysis frequencies, and dry deposition, may also

376   benefit from the parameterized R_{eff}. Further developments in computational efficiency of aerosol microphysics models

377   and more abundant measurements of aerosol size and optical properties would both offer opportunities for further

378   advances.

379

Data availability. AERONET data can be found at https://aeronet.gsfc.nasa.gov/. Aircraft data during DISCOVER-AQ are available at https://asdc.larc.nasa.gov/project/DISCOVER-AQ. KORUS-AQ data can be found at https://doi.org/10.5067/Suborbital/KORUSAQ/DATA01.

Author contributions. HZ and RVM designed the study. HZ performed the data analysis and model simulations with contributions from BC, SZ, CL, LB, JRP, IS, DC, and RYWC. BEA, LDZ, JWH, RAF, CAH, JLJ, PCJ, JED, JSS, AW, and BAN contributed to KORUS-AQ and DISCOVER-AQ campaign measurements. HZ and RVM wrote the paper with input from all authors.

Competing interests. The contact author has declared that neither they nor their co-authors have any competing interests.

Financial support. This work was supported by NASA Grant 80NSSC21K1343. JRP was funded by the US NSF Atmospheric Chemistry program, under grant AGS-1950327. JLJ and PCJ were supported by NASA Grant 80NSSC21K1451 and NNX15AT96G. BAN was supported by NASA Grant 80NSSC22K0283. JED was supported by NASA Grant NNX15AT88G.

Appendix A

A1 Application of spatially and temporally varying OM/OC ratio

The top panel of Figure A1 shows scatter plots of the estimated and measured OM/OC and OM during the KORUS-AQ campaign. The estimation is obtained by applying to OC measurement a NO_2 inferred OM/OC from Philip et al. (2014), with a subsequent correction factor of 1.09 suggested by Canagaratna et al. (2015). Estimated OM is compared with measured OM by AMS during the campaign. Overall consistency is evident between NO_2-derived OM/OC and measured OM/OC. The agreement is better below 500 m than above (left panel, $R^2 = 0.62$ vs. 0.33). The discrepancy at high altitudes is mainly due to the low NO_2 (<0.2 ppbv), where the Philip *et al.* (2014) equation is not applicable. An average OM/OC ratio (2.1) is applied in this case. A high degree of consistency exists between the estimated OM and measured OM, with $R^2 = 0.99$ and slope = 0.91 for data from all altitudes (right panel), thus supporting the use of estimated OM in our analyses. The bottom left panel compares the vertical profile of the estimates and measurements, yielding overall consistency.

405
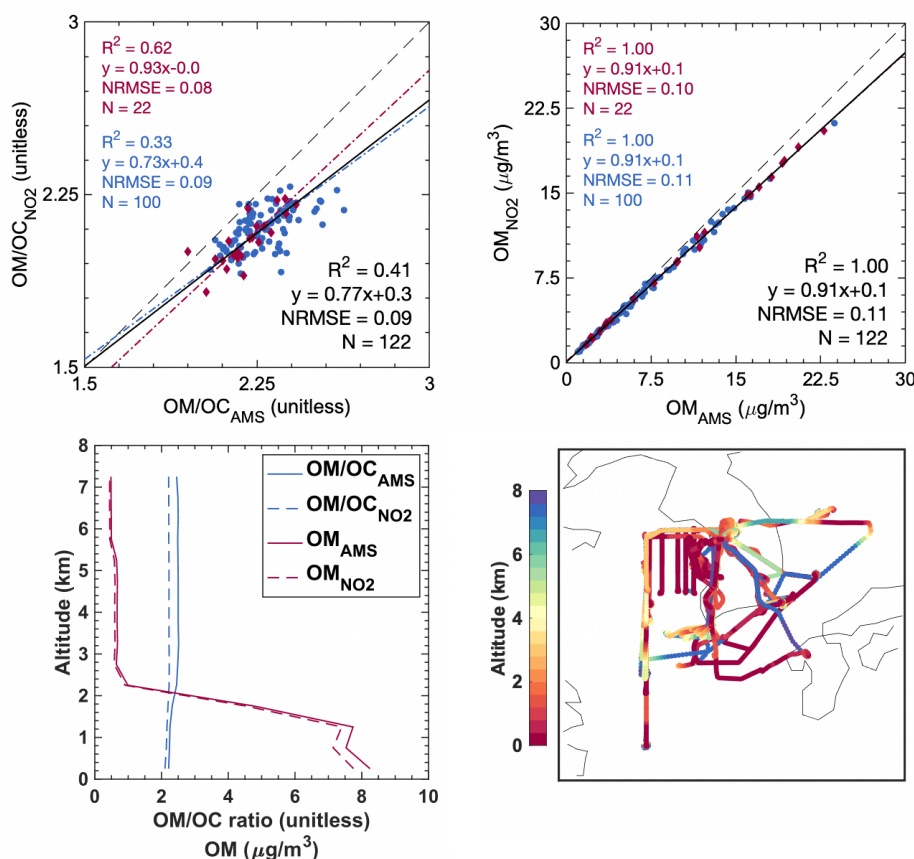
Figure A1. Scatter plots of estimated and measured OM/OC (top left) and OM (top right) during KORUS-AQ. Each point represents a mean value of AMS measurement for a 1-hour interval. Red diamonds, lines, and texts represent data from 0-500 m altitude. Blue dots, lines, and text represent data above 500 m from the ground. Black solid lines and texts represent the line of best fit for all the data. The 1:1 line is dashed. NRMSD is the normalized root mean square deviation between the two datasets. N is the number of points in each dataset. (Bottom left) Mean values of OM/OC and OM from measurements and estimations along the altitude. (Bottom right) Flight tracks during KORUS-AQ.

A2 Aerosol Extinction Calculation in GEOS-Chem

Extinction (Ext) of radiation by aerosols is represented as the sum of extinction due to each of the aerosol components using the following equation:

$$Ext_k = \frac{3Q_{ext,k}M_k}{4\rho_k R_{eff,k}}$$

Eqn. (3)

where subscript k indicates the property for the kth component. R_{eff} is the effective radius defined as the area weighted mean radius. Q_{ext} is the area-weighted mean extinction efficiency. M is the aerosol mass loading per unit volume. ρ is the aerosol density. Aerosol optical depth (AOD) is the integral of aerosol extinction across the vertical domain.

For each component, extinction is calculated for assumed log-normal size distribution with corresponding dry geometric mean radius R_g and geometric standard deviation σ, hygroscopicity, refractive index (RI), and density (ρ) for individual aerosol components, as listed in Table A1. Sulfate, nitrate, and ammonium are grouped into SNA for convenience. R_{eff} and Q_{ext} are calculated using Mie Theory (Mishchenko et al., 1999, 2002) based on assumptions in aerosol size and RI. Hygroscopicity for SNA and OM is represented using a κ-Kohler hygroscopic growth scheme (Kreidenweis et al., 2008) as implemented by Latimer & Martin (2019).

Table A1. Dry aerosol properties in GEOS-Chem bulk model

Aerosol components	R_g, μm	σ	Hygroscopicity	Refractive Index (dry, 550 nm)	ρ, g cm^{-3}	R_{eff}, μm	Q_{ext}
SNA	0.058	1.6	$\kappa = 0.61$	$1.53 - 6.0\times10^{-3}$i	1.7	0.101	0.603
OM	0.058	1.6	$\kappa = 0.1$	$1.53 - 6.0\times10^{-3}$i	1.3	0.101	0.603

428 **Appendix B**
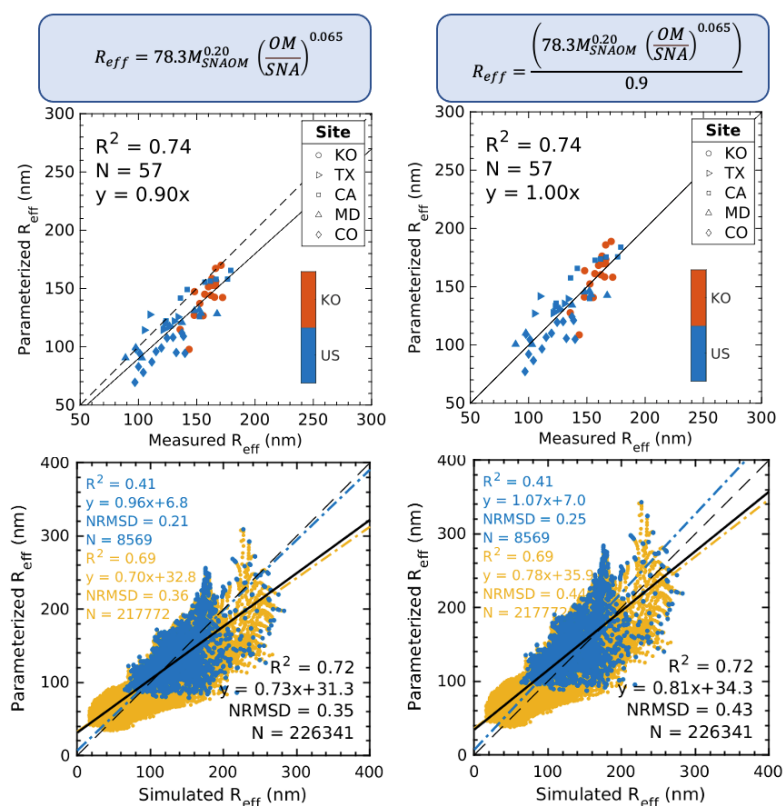
429

430 **Figure B1. (Top) Scatter plot of parameterized R_{eff} and measured R_{eff} from DISCOVER-**

431 **AQ and KORUS-AQ. Each point represents a daily mean measurement. (Bottom) Scatter plot of parameterized R_{eff} and**

432 **GEOS-Chem-TOMAS simulated R_{eff} for the planetary boundary layer (blue dots, line, and texts), and for the**

433 **free troposphere (yellow dots, line, and texts). Black solid lines and the texts indicate the entire troposphere**

434 **with the sum of SNA and OM > 90% of aerosol mass. The 1:1 line is dashed. NRMSD is the normalized root**

435 **mean square deviation between the two datasets. N is the number of points in each dataset. The left panel**

436 **indicates the original parameterization from multiple linear regression. The right panel shows the adjusted**

437 **parameterization using aircraft measurements.**

438
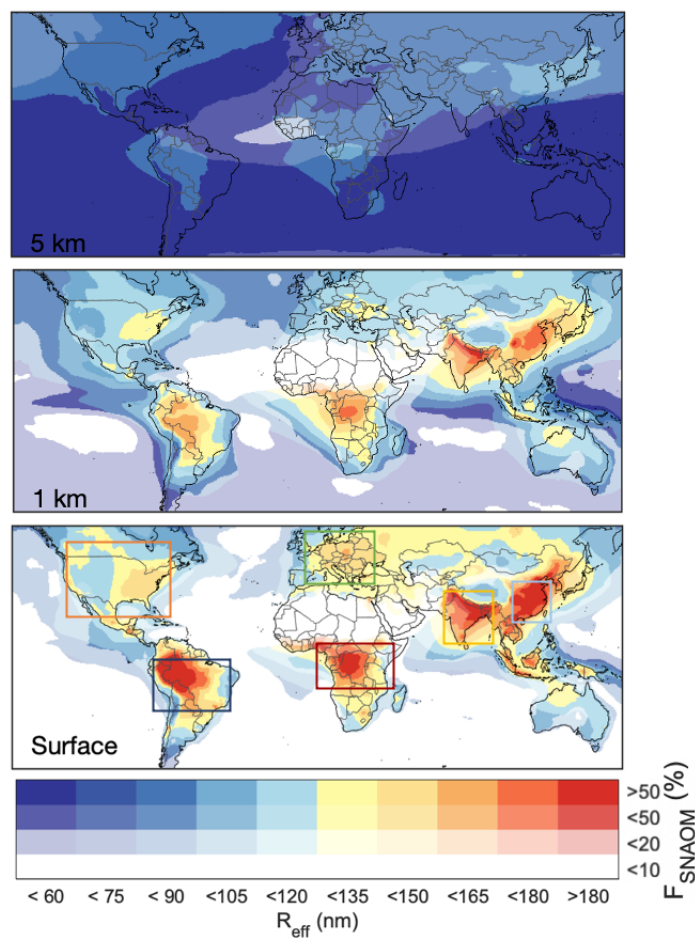
Figure B2. Annual mean R_{eff} for SNA and OM at (top) about 5 km, (middle) about 1 km, and (bottom)
439

surface, calculated using Eqn. (5) and simulated SNA and OM mass from GEOS-Chem bulk model. F_{SNAOM} is
440

the ratio of SNA and OM mass to the total aerosol mass. Boxes in the bottom panel define regions referred to
441
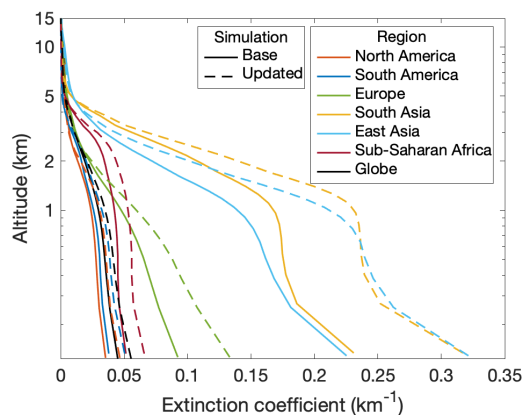
by Figure B3.
442

Figure B3. Global and regional aerosol extinction coefficient simulated by GEOS-Chem bulk model with original R_eff (solid lines) and parameterized R_eff (dashed lines). Regions are defined by the boxes in Figure B2.
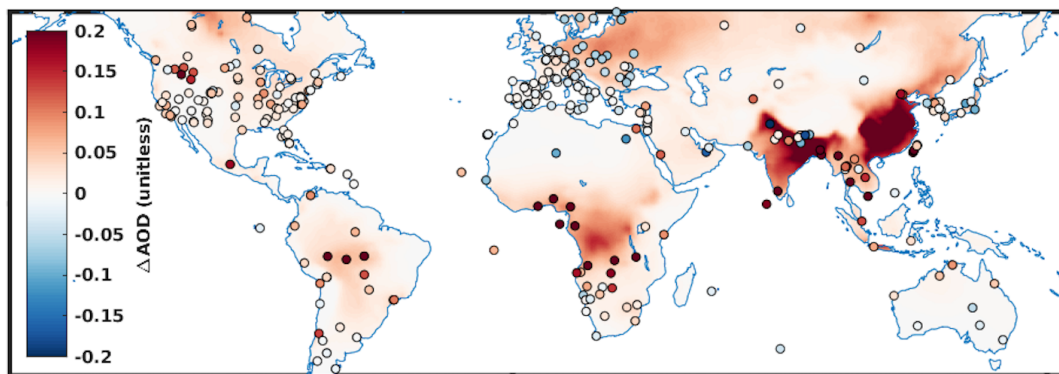
Figure B4. Difference between AERONET AOD minus default GEOS-Chem simulated AOD (dots) and difference between simulated AOD with the parameterized R_eff minus AOD with default R_eff (background).

Reference

Aalto, P., Hämeri, K., Becker, E. D. O., Weber, R., Salm, J., Mäkelä, J. M., et al. (2001). Physical characterization of aerosol particles during nucleation events. *Tellus, Series B: Chemical and Physical Meteorology*, *53*(4), 344–358. https://doi.org/10.3402/tellusb.v53i4.17127

AboEl-Fetouh, Y., O'Neill, N. T., Kodros, J. K., Pierce, J. R., Lu, H., Ranjbar, K., & Xian, P. (2022). Seasonal comparisons of GEOS-Chem-TOMAS (GCT) simulations with AERONET-inversion retrievals over sites in the North American and European Arctic. *Atmospheric Environment*, *271*, 118852. https://doi.org/https://doi.org/10.1016/j.atmosenv.2021.118852

Adams, P. J., & Seinfeld, J. H. (2002). Predicting global aerosol size distributions in general circulation models. *Journal of Geophysical Research Atmospheres*, *107*(19), AAC 4-1-AAC 4-23. https://doi.org/10.1029/2001JD001010

Adams, P. J., & Seinfeld, J. H. (2003). Disproportionate impact of particulate emissions on global cloud condensation nuclei concentrations. *Geophysical Research Letters*, *30*(5), 1–4. https://doi.org/10.1029/2002gl016303

Andreae, M. O., Acevedo, O. C., Araùjo, A., Artaxo, P., Barbosa, C. G. G., Barbosa, H. M. J., et al. (2015). The Amazon Tall Tower Observatory (ATTO): Overview of pilot measurements on ecosystem ecology, meteorology, trace gases, and aerosols. *Atmospheric Chemistry and Physics*, *15*(18), 10723–10776. https://doi.org/10.5194/acp-15-10723-2015

Bahreini, R., Jimenez, J. L., Wang, J., Flagan, R. C., Seinfeld, J. H., Jayne, J. T., & Worsnop, D. R. (2003). Aircraft-based aerosol size and composition measurements during ACE-Asia using an Aerodyne aerosol mass spectrometer. *Journal of Geophysical Research: Atmospheres*, *108*(23). https://doi.org/10.1029/2002jd003226

Bey, I., Jacob, D. J., Yantosca, R. M., Logan, J. A., Field, B. D., Fiore, A. M., et al. (2001). Global modeling of tropospheric chemistry with assimilated meteorology: Model description and evaluation. *Journal of Geophysical Research Atmospheres*, *106*(D19), 23073–23095. https://doi.org/10.1029/2001JD000807

Bindle, L., Martin, R. V., Cooper, M. J., Lundgren, E. W., Eastham, S. D., Auer, B. M., et al. (2021). Grid-stretching capability for the GEOS-Chem 13.0.0 atmospheric chemistry model. *Geoscientific Model Development*, *14*(10), 5977–5997. https://doi.org/10.5194/gmd-14-5977-2021

Canagaratna, M. R., Jayne, J. T., Jimenez, J. L., Allan, J. D., Alfarra, M. R., Zhang, Q., et al. (2007). Chemical and microphysical characterization of ambient aerosols with the aerodyne aerosol mass spectrometer. *Mass Spectrometry Reviews*, *26*(2), 185–222.

Canagaratna, M. R., Jimenez, J. L., Kroll, J. H., Chen, Q., Kessler, S. H., Massoli, P., et al. (2015). Elemental ratio measurements of organic compounds using aerosol mass spectrometry: Characterization, improved calibration, and implications. *Atmospheric Chemistry and Physics*, *15*(1), 253–272. https://doi.org/10.5194/acp-15-253-2015

Choi, S., Lamsal, L. N., Follette-Cook, M., Joiner, J., Krotkov, N. A., Swartz, W. H., et al. (2020). Assessment of NO2 observations during DISCOVER-AQ and KORUS-AQ field campaigns. *Atmospheric Measurement Techniques*, *13*(5), 2523–2546. https://doi.org/10.5194/amt-13-2523-2020

Chu, D. A., Ferrare, R., Szykman, J., Lewis, J., Scarino, A., Hains, J., et al. (2015). Regional characteristics of the relationship between columnar AOD and surface PM2.5: Application of lidar aerosol extinction profiles over Baltimore-Washington Corridor during DISCOVER-AQ. *Atmospheric Environment*, *101*, 338e349-349. https://doi.org/10.1016/j.atmosenv.2014.11.034

Croft, B., Lohmann, U., & von Salzen, K. (2005). Black carbon ageing in the Canadian Centre for Climate modelling and analysis atmospheric general circulation model. *Atmospheric Chemistry and Physics*, *5*(7), 1931–1949. https://doi.org/10.5194/acp-5-1931-2005

D'Andrea, S. D., Häkkinen, S. A. K., Westervelt, D. M., Kuang, C., Levin, E. J. T., Kanawade, V. P., et al. (2013). Understanding global secondary organic aerosol amount and size-resolved condensational behavior. *Atmospheric Chemistry and Physics*, *13*(22), 11519–11534. https://doi.org/10.5194/acp-13-11519-2013

Dibb, J. E., Talbot, R. W., Scheuer, E. M., Seid, G., Avery, M. A., & Singh, H. B. (2003). Aerosol chemical

496   composition in Asian continental outflow during the TRACE-P campaign: Comparison with PEM-West B.
497   *Journal of Geophysical Research: Atmospheres*, *108*(21). https://doi.org/10.1029/2002jd003111

498   Fairlie D., T., Jacob, D. J., & Park, R. J. (2007). The impact of transpacific transport of mineral dust in the United
499   States. *Atmospheric Environment*, *41*(6), 1251–1266. https://doi.org/10.1016/j.atmosenv.2006.09.048

500   Eastham, S. D., Long, M. S., Keller, C. A., Lundgren, E., Yantosca, R. M., Zhuang, J., et al. (2018). GEOS-Chem
501   high performance (GCHP v11-02c): A next-generation implementation of the GEOS-Chem chemical transport
502   model for massively parallel applications. *Geoscientific Model Development*, *11*(7), 2941–2953.
503   https://doi.org/10.5194/gmd-11-2941-2018

504   Emerson, E. W., Hodshire, A. L., DeBolt, H. M., Bilsback, K. R., Pierce, J. R., McMeeking, G. R., & Farmer, D. K.
505   (2020). Revisiting particle dry deposition and its role in radiative effect estimates. *Proceedings of the National
506   Academy of Sciences of the United States of America*, *117*(42), 26076–26082.
507   https://doi.org/10.1073/pnas.2014761117

508   Ervens, B., Turpin, B. J., & Weber, R. J. (2011). Secondary organic aerosol formation in cloud droplets and aqueous
509   particles (aqSOA): A review of laboratory, field and model studies. *Atmospheric Chemistry and Physics*, *11*(21),
510   11069–11102. https://doi.org/10.5194/acp-11-11069-2011

511   Estillore, A. D., Trueblood, J. V., & Grassian, V. H. (2016). Atmospheric chemistry of bioaerosols: Heterogeneous
512   and multiphase reactions with atmospheric oxidants and other trace gases. *Chemical Science*, *7*(11), 6604–6616.
513   https://doi.org/10.1039/c6sc02353c

514   Faxvog, F. R., & Roessler, D. M. (1978). Carbon aerosol visibility vs particle size distribution. *Applied Optics*, *17*(16),
515   2612. https://doi.org/10.1364/ao.17.002612

516   Fountoukis, C., & Nenes, A. (2007). ISORROPIAII: A computationally efficient thermodynamic equilibrium model
517   for K+-Ca2+-Mg2+-NH4+-Na+-SO42--NO3--Cl--H2O aerosols. *Atmospheric Chemistry and Physics*, *7*(17),
518   4639–4659. https://doi.org/10.5194/acp-7-4639-2007

519   Giles, D. M., Sinyuk, A., Sorokin, M. G., Schafer, J. S., Smirnov, A., Slutsker, I., et al. (2019). Advancements in the
520   Aerosol Robotic Network (AERONET) Version 3 database - Automated near-real-time quality control
521   algorithm with improved cloud screening for Sun photometer aerosol optical depth (AOD) measurements.
522   *Atmospheric Measurement Techniques*, *12*(1), 169–209. https://doi.org/10.5194/amt-12-169-2019

523   Guo, H., Campuzano-Jost, P., Nault, B. A., Day, D. A., Schroder, J. C., Kim, D., et al. (2021). The importance of size
524   ranges in aerosol instrument intercomparisons: A case study for the Atmospheric Tomography Mission.
525   *Atmospheric Measurement Techniques*, *14*(5), 3631–3655. https://doi.org/10.5194/amt-14-3631-2021

526   Hair, J. W., Hostetler, C. A., Cook, A. L., Harper, D. B., Ferrare, R. A., Mack, T. L., et al. (2008). Airborne High
527   Spectral Resolution Lidar for profiling Aerosol optical properties. *Applied Optics*, *47*(36), 6734–6753.
528   https://doi.org/10.1364/AO.47.006734

529   Hammer, M. S., Martin, R. V., Van Donkelaar, A., Buchard, V., Torres, O., Ridley, D. A., & Spurr, R. J. D. (2016).
530   Interpreting the ultraviolet aerosol index observed with the OMI satellite instrument to understand absorption
531   by organic aerosols: Implications for atmospheric oxidation and direct radiative effects. *Atmospheric Chemistry
532   and Physics*, *16*(4), 2507–2523. https://doi.org/10.5194/acp-16-2507-2016

533   Hansen, J. E., & Travis, L. D. (1974). Light scattering in planetary atmospheres. *Space Science Reviews*, *16*(4), 527–
534   610. https://doi.org/10.1007/BF00168069

535   Hayes, P. L., Ortega, A. M., Cubison, M. J., Froyd, K. D., Zhao, Y., Cliff, S. S., et al. (2013). Organic aerosol
536   composition and sources in Pasadena, California, during the 2010 CalNex campaign. *Journal of Geophysical
537   Research Atmospheres*, *118*(16), 9233–9257. https://doi.org/10.1002/jgrd.50530

538   Hinds, W. C., & Zhu, Y. (1999). *Aerosol technology: Properties, behavior, and measurement of airborne particles*
539   (Second). New York: Wiley.

540   Huang, Y., Li, L., Li, J., Wang, X., Chen, H., Chen, J., et al. (2013). A case study of the highly time-resolved evolution
541   of aerosol chemical and optical properties in urban Shanghai, China. *Atmospheric Chemistry and Physics*, *13*(8),
542   3931–3944. https://doi.org/10.5194/acp-13-3931-2013

543   Jaeglé, L., Quinn, P. K., Bates, T. S., Alexander, B., & Lin, J. T. (2011). Global distribution of sea salt aerosols: New
544   constraints from in situ and remote sensing observations. *Atmospheric Chemistry and Physics*, *11*(7), 3137–
545   3157. https://doi.org/10.5194/acp-11-3137-2011

546   Janḧall, S., Andreae, M. O., & Pöschl, U. (2010). Biomass burning aerosol emissions from vegetation fires: Particle
547   number and mass emission factors and size distributions. *Atmospheric Chemistry and Physics*, *10*(3), 1427–
548   1439. https://doi.org/10.5194/acp-10-1427-2010

549   Jin, J., Henzing, B., & Segers, A. (2022). How aerosol size matters in AOD assimilation and the optimization using
550   Ångström exponent. *Atmospheric Chemistry and Physics Discussions*, *2022*, 1–30. https://doi.org/10.5194/acp-
551   2022-630

552   Jordan, C. E., Crawford, J. H., Beyersdorf, A. J., Eck, T. F., Halliday, H. S., Nault, B. A., et al. (2020). Investigation
553   of factors controlling PM2. 5 variability across the South Korean Peninsula during KORUS-AQ. *Elementa:*
554   *Science of the Anthropocene*, *8*.

555   Kahn, R. A., Gaitley, B. J., Martonchik, J. V., Diner, D. J., Crean, K. A., & Holben, B. (2005). Multiangle Imaging
556   Spectroradiometer (MISR) global aerosol optical depth validation based on 2 years of coincident Aerosol
557   Robotic Network (AERONET) observations. *Journal of Geophysical Research D: Atmospheres*, *110*(10), 1–16.
558   https://doi.org/10.1029/2004JD004706

559   Karydis, V. A., Kumar, P., Barahona, D., Sokolik, I. N., & Nenes, A. (2011). On the effect of dust particles on global
560   cloud condensation nuclei and cloud droplet number. *Journal of Geophysical Research Atmospheres*, *116*(23).
561   https://doi.org/10.1029/2011JD016283

562   Kellogg, W. W. (1980). Aerosols and Climate. *Science*, *183*(4120), 281–296.
563   https://doi.org/10.1093/oso/9780198779308.003.0005

564   Kodros, J. K., & Pierce, J. R. (2017). Important global and regional differences in aerosol cloud-albedo effect estimates
565   between simulations with and without prognostic aerosol microphysics. *Journal of Geophysical Research*,
566   *122*(7), 4003–4018. https://doi.org/10.1002/2016JD025886

567   Kodros, J. K., Volckens, J., Jathar, S. H., & Pierce, J. R. (2018). Ambient particulate matter size distributions drive
568   regional and global variability in particle deposition in the respiratory tract. *GeoHealth*, *2*(10), 298–312.
569   https://doi.org/10.1029/2018gh000145

570   Koffi, B., Schulz, M., Bréon, F. M., Dentener, F., Steensen, B. M., Griesfeller, J., et al. (2016). Evaluation of the
571   aerosol vertical distribution in global aerosol models through comparison against CALIOP measurements:
572   AeroCom phase II results. *Journal of Geophysical Research*, *121*(12), 7254–7283.
573   https://doi.org/10.1002/2015JD024639

574   Kopke P., H. M. S. I. S. E. P. (1997). *Aerosol data set. Max Planck Institut fur Meteorologie, Report No. 243* (Vol.
575   243). Hamburg. https://doi.org/Report No. 243

576   Kreidenweis, S. M., Petters, M. D., & DeMott, P. J. (2008). Single-parameter estimates of aerosol water content.
577   *Environmental Research Letters*, *3*(3), 35002.

578   Lamarque, J. F., Shindell, D. T., Josse, B., Young, P. J., Cionni, I., Eyring, V., et al. (2013). The atmospheric chemistry
579   and climate model intercomparison Project (ACCMIP): Overview and description of models, simulations and
580   climate diagnostics. *Geoscientific Model Development*, *6*(1), 179–206. https://doi.org/10.5194/gmd-6-179-2013

581   Lamb, K. D., Perring, A. E., Samset, B., Peterson, D., Davis, S., Anderson, B. E., et al. (2018). Estimating Source
582   Region Influences on Black Carbon Abundance, Microphysics, and Radiative Effect Observed Over South
583   Korea. *Journal of Geophysical Research: Atmospheres*, *123*(23), 13,527-13,548.
584   https://doi.org/10.1029/2018JD029257

585   Latimer, R. N. C., & Martin, R. V. (2019). Interpretation of measured aerosol mass scattering efficiency over North
586   America using a chemical transport model. *Atmospheric Chemistry and Physics*, *19*(4), 2635–2653.
587   https://doi.org/10.5194/acp-19-2635-2019

588   Lee, Y. N., Weber, R., Ma, Y., Orsini, D., Maxwell-Meier, K., Blake, D., et al. (2003). Airborne measurement of
589   inorganic ionic components of fine aerosol particles using the particle-into-liquid sampler coupled to ion
590   chromatography technique during ACE-Asia and TRACE-P. *Journal of Geophysical Research: Atmospheres*,

591 *108*(23). https://doi.org/10.1029/2002jd003265

592 Levy, R. C., Mattoo, S., Munchak, L. A., Remer, L. A., Sayer, A. M., Patadia, F., & Hsu, N. C. (2013). The Collection
593   6 MODIS aerosol products over land and ocean. *Atmospheric Measurement Techniques*, *6*(11), 2989–3034.
594   https://doi.org/10.5194/amt-6-2989-2013

595 Liu, H., Jacob, D. J., Bey, I., & Yantosca, R. M. (2001). Constraints from 210Pb and 7Be on wet deposition and
596   transport in a global three-dimensional chemical tracer model driven by assimilated meteorological fields.
597   *Journal   of   Geophysical   Research   Atmospheres*,   *106*(D11),   12109–12128.
598   https://doi.org/10.1029/2000JD900839

599 Liu, X., Easter, R. C., Ghan, S. J., Zaveri, R., Rasch, P., Shi, X., et al. (2012). Toward a minimal representation of
600   aerosols in climate models: Description and evaluation in the Community Atmosphere Model CAM5.
601   *Geoscientific Model Development*, *5*(3), 709–739. https://doi.org/10.5194/gmd-5-709-2012

602 Liu, X., Ma, P.-L., Wang, H., Tilmes, S., Singh, B., Easter, R. C., et al. (2016). Description and evaluation of a new
603   four-mode version of the Modal Aerosol Module (MAM4) within version 5.3 of the Community Atmosphere
604   Model. *Geoscientific Model Development*, *9*(2), 505–522.

605 Malm, W. C., Sisler, J. F., Huffman, D., Eldred, R. A., & Cahill, T. A. (1994). Spatial and seasonal trends in particle
606   concentration and optical extinction in the United States. *Journal of Geophysical Research*, *99*(D1), 1347–1370.
607   https://doi.org/10.1029/93JD02916

608 Mann, G. W., Carslaw, K. S., Spracklen, D. V., Ridley, D. A., Manktelow, P. T., Chipperfield, M. P., et al. (2010).
609   Description and evaluation of GLOMAP-mode: A modal global aerosol microphysics model for the UKCA
610   composition-climate model. *Geoscientific Model Development*, *3*(2), 519–551. https://doi.org/10.5194/gmd-3-
611   519-2010

612 Marais, E. A., Jacob, D. J., Jimenez, J. L., Campuzano-Jost, P., Day, D. A., Hu, W., et al. (2016). Aqueous-phase
613   mechanism for secondary organic aerosol formation from isoprene: Application to the southeast United States
614   and co-benefit of SO2 emission controls. *Atmospheric Chemistry and Physics*, *16*(3), 1603–1618.
615   https://doi.org/10.5194/acp-16-1603-2016

616 Martin, R. V., Jacob, D. J., Yantosca, R. M., Chin, M., & Ginoux, P. (2003). Global and regional decreases in
617   tropospheric oxidants from photochemical effects of aerosols. *Journal of Geophysical Research: Atmospheres*,
618   *108*(3). https://doi.org/10.1029/2002jd002622

619 Martin, R. V, Eastham, S. D., Bindle, L., Lundgren, E. W., Clune, T. L., Keller, C. A., et al. (2022). Improved
620   Advection , Resolution , Performance , and Community Access in the New Generation (Version 13) of the
621   High Performance GEOS-Chem Global Atmospheric Chemistry Model (GCHP). *Geoscientific Model*
622   *Development Discussions*, *720*(February), 1–30. https://doi.org/10.5194/gmd-2022-42

623 McDuffie, E. E., Smith, S. J., O'Rourke, P., Tibrewal, K., Venkataraman, C., Marais, E. A., et al. (2020). A global
624   anthropogenic emission inventory of atmospheric pollutants from sector- And fuel-specific sources (1970-2017):
625   An application of the Community Emissions Data System (CEDS). *Earth System Science Data*, *12*(4), 3413–
626   3442. https://doi.org/10.5194/essd-12-3413-2020

627 McDuffie, E. E., Martin, R. V., Spadaro, J. V., Burnett, R., Smith, S. J., O'Rourke, P., et al. (2021). Source sector and
628   fuel contributions to ambient PM2.5 and attributable mortality across multiple spatial scales. *Nature*
629   *Communications*, *12*(1), 1–12. https://doi.org/10.1038/s41467-021-23853-y

630 McNaughton, C. S., Clarke, A. D., Howell, S. G., Pinkerton, M., Anderson, B., Thornhill, L., et al. (2007). Results
631   from the DC-8 inlet characterization experiment (DICE): Airborne versus surface sampling of mineral dust and
632   sea   salt   aerosols.   *Aerosol   Science   and   Technology*,   *41*(2),   136–159.
633   https://doi.org/10.1080/02786820601118406

634 Meng, J., Martin, R. V., Ginoux, P., Hammer, M., Sulprizio, M. P., Ridley, D. A., & Van Donkelaar, A. (2021). Grid-
635   independent high-resolution dust emissions (v1.0) for chemical transport models: Application to GEOS-Chem
636   (12.5.0). *Geoscientific Model Development*, *14*(7), 4249–4260. https://doi.org/10.5194/gmd-14-4249-2021

637 Mishchenko, M. I., Dlugach, J. M., Yanovitskij, E. G., & Zakharova, N. T. (1999). Bidirectional reflectance of flat,
638   optically thick particulate layers: An efficient radiative transfer solution and applications to snow and soil

surfaces. *Journal of Quantitative Spectroscopy and Radiative Transfer*, *63*(2–6), 409–432. https://doi.org/10.1016/S0022-4073(99)00028-X

Mishchenko, M. I., Travis, L. D., & Lacis, A. a. (2002). *Scattering, Absorption, and Emission of Light by Small Particles*. *Vasa*. Cambridge: Cambridge University Press.

Moore, R. H., Wiggins, E. B., Ahern, A. T., Zimmerman, S., Montgomery, L., Campuzano Jost, P., et al. (2021). Sizing response of the Ultra-High Sensitivity Aerosol Spectrometer (UHSAS) and Laser Aerosol Spectrometer (LAS) to changes in submicron aerosol composition and refractive index. *Atmospheric Measurement Techniques*, *14*(6), 4517–4542. https://doi.org/10.5194/amt-14-4517-2021

Napari, I., Noppel, M., Vehkamäki, H., & Kulmala, M. (2002). Parametrization of ternary nucleation rates for H2so4-NH3-H2O vapors. *Journal of Geophysical Research Atmospheres*, *107*(19), AAC 6-1-AAC 6-6. https://doi.org/10.1029/2002JD002132

Nault, B. A., Campuzano-Jost, P., Day, D. A., Schroder, J. C., Anderson, B., Beyersdorf, A. J., et al. (2018). Secondary organic aerosol production from local emissions dominates the organic aerosol budget over Seoul, South Korea, during KORUS-AQ. *Atmospheric Chemistry and Physics*, *18*(24), 17769–17800. https://doi.org/10.5194/acp-18-17769-2018

Ngo, N. S., Asseko, S. V. J., Ebanega, M. O., Allo'o Allo'o, S. M., & Hystad, P. (2019). The relationship among PM2.5, traffic emissions, and socioeconomic status: Evidence from Gabon using low-cost, portable air quality monitors. *Transportation Research Part D: Transport and Environment*, *68*, 2–9. https://doi.org/10.1016/j.trd.2018.01.029

Park, R. J. (2004). Natural and transboundary pollution influences on sulfate-nitrate-ammonium aerosols in the United States: Implications for policy. *Journal of Geophysical Research*, *109*(D15). https://doi.org/10.1029/2003jd004473

Park, R. J., Jacob, D. J., Chin, M., & Martin, R. V. (2003). Sources of carbonaceous aerosols over the United States and implications for natural visibility. *Journal of Geophysical Research Atmospheres*, *108*(12). https://doi.org/10.1029/2002jd003190

Philip, S., Martin, R. V., Pierce, J. R., Jimenez, J. L., Zhang, Q., Canagaratna, M. R., et al. (2014). Spatially and seasonally resolved estimate of the ratio of organic mass to organic carbon. *Atmospheric Environment*, *87*, 34–40. https://doi.org/10.1016/j.atmosenv.2013.11.065

Philip, S., Martin, R. V., Snider, G., Weagle, C. L., Van Donkelaar, A., Brauer, M., et al. (2017). Anthropogenic fugitive, combustion and industrial dust is a significant, underrepresented fine particulate matter source in global atmospheric models. *Environmental Research Letters*, *12*(4). https://doi.org/10.1088/1748-9326/aa65a4

Pierce, J. R., Chen, K., & Adams, P. J. (2007). Contribution of primary carbonaceous aerosol to cloud condensation nuclei: Processes and uncertainties evaluated with a global aerosol microphysics model. *Atmospheric Chemistry and Physics*, *7*(20), 5447–5466. https://doi.org/10.5194/acp-7-5447-2007

Pierce, J. R., Croft, B., Kodros, J. K., D'Andrea, S. D., & Martin, R. V. (2015). The importance of interstitial particle scavenging by cloud droplets in shaping the remote aerosol size distribution and global aerosol-climate effects. *Atmospheric Chemistry and Physics*, *15*(11), 6147–6158. https://doi.org/10.5194/acp-15-6147-2015

Plaza, J., Pujadas, M., Gómez-Moreno, F. J., Sánchez, M., & Artíñano, B. (2011). Mass size distributions of soluble sulfate, nitrate and ammonium in the Madrid urban aerosol. *Atmospheric Environment*, *45*(28), 4966–4976.

Podolske, J. R., Sachse, G. W., & Diskin, G. S. (2003). Calibration and data retrieval algorithms for the NASA Langley/Ames Diode Laser Hygrometer for the NASA Transport and Chemical Evolution over the Pacific (TRACE-P) mission. *Journal of Geophysical Research: Atmospheres*, *108*(20). https://doi.org/10.1029/2002jd003156

Pye, H. O. T., Chan, A. W. H., Barkley, M. P., & Seinfeld, J. H. (2010). Global modeling of organic aerosol: The importance of reactive nitrogen (NOx and NO3). *Atmospheric Chemistry and Physics*, *10*(22), 11261–11276. https://doi.org/10.5194/acp-10-11261-2010

Ramnarine, E., Kodros, J. K., Hodshire, A. L., Lonsdale, C. R., Alvarado, M. J., & Pierce, J. R. (2019). Effects of near-source coagulation of biomass burning aerosols on global predictions of aerosol size distributions and

687   implications for aerosol radiative effects. *Atmospheric Chemistry and Physics*, *19*(9), 6561–6577.
688   https://doi.org/10.5194/acp-19-6561-2019

689   Reid, J. S., Eck, T. F., Christopher, S. A., Koppman, R., Dubovik, O., Eleuterio, D. P., et al. (2005). A review of
690   biomass burning emissions part III: Intensive optical properties of biomass burning particles. *Atmospheric*
691   *Chemistry and Physics*, *5*(3), 827–849. https://doi.org/10.5194/acp-5-827-2005

692   Remoundaki, E., Kassomenos, P., Mantas, E., Mihalopoulos, N., & Tsezos, M. (2013). Composition and mass closure
693   of PM2.5 in urban environment (Athens, Greece). *Aerosol and Air Quality Research*, *13*(1), 72–82.
694   https://doi.org/10.4209/aaqr.2012.03.0054

695   Reutter, P., Su, H., Trentmann, J., Simmel, M., Rose, D., Gunthe, S. S., et al. (2009). Aerosol- and updraft-limited
696   regimes of cloud droplet formation: Influence of particle number, size and hygroscopicity on the activation of
697   cloud condensation nuclei (CCN). *Atmospheric Chemistry and Physics*, *9*(18), 7067–7080.
698   https://doi.org/10.5194/acp-9-7067-2009

699   Rissler, J., Vestin, A., Swietlicki, E., Fisch, G., Zhou, J., Artaxo, P., & Andreae, M. O. (2006). Size distribution and
700   hygroscopic properties of aerosol particles from dry-season biomass burning in Amazonia. *Atmospheric*
701   *Chemistry and Physics*, *6*(2), 471–491. https://doi.org/10.5194/acp-6-471-2006

702   Rodríguez, S., Van Dingenen, R., Putaud, J. P., Dell'Acqua, A., Pey, J., Querol, X., et al. (2007). A study on the
703   relationship between mass concentrations, chemistry and number size distribution of urban fine aerosols in
704   Milan, Barcelona and London. *Atmospheric Chemistry and Physics*, *7*(9), 2217–2232.
705   https://doi.org/10.5194/acp-7-2217-2007

706   Ruijrok, W., Davidson, C. I., & Nicholson, K. W. (1995). Dry deposition of particles. *Tellus B*, *47*(5), 587–601.
707   https://doi.org/10.1034/j.1600-0889.47.issue5.6.x

708   Sakamoto, K. M., Laing, J. R., Stevens, R. G., Jaffe, D. A., & Pierce, J. R. (2016). The evolution of biomass-burning
709   aerosol size distributions due to coagulation: Dependence on fire and meteorological details and
710   parameterization. *Atmospheric Chemistry and Physics*, *16*(12), 7709–7724. https://doi.org/10.5194/acp-16-
711   7709-2016

712   Sawamura, P., Moore, H. R., Burton, P. S., Chemyakin, E., Müller, D., Kolgotin, A., et al. (2017). HSRL-2 aerosol
713   optical measurements and microphysical retrievals vs. airborne in situ measurements during DISCOVER-AQ
714   2013: An intercomparison study. *Atmospheric Chemistry and Physics*, *17*(11), 7229–7243.
715   https://doi.org/10.5194/acp-17-7229-2017

716   Schubert, S. D., Rood, R. B., & Pfaendtner, J. (1993). An Assimilated Dataset for Earth Science Applications. *Bulletin*
717   *of the American Meteorological Society*, *74*(12), 2331–2342. https://doi.org/10.1175/1520-
718   0477(1993)074<2331:AADFES>2.0.CO;2

719   Schwarz, J. P., Gao, R. S., Fahey, D. W., Thomson, D. S., Watts, L. A., Wilson, J. C., et al. (2006). Single-particle
720   measurements of midlatitude black carbon and light-scattering aerosols from the boundary layer to the lower
721   stratosphere. *Journal of Geophysical Research: Atmospheres*, *111*(D16).

722   Seinfeld, J. H., & Pandis, S. N. (2016). *Atmospheric Chemistry and Physics* (Third). New York: John Wiley.

723   Shah, V., Jacob, D. J., Moch, J. M., Wang, X., & Zhai, S. (2020). Global modeling of cloud water acidity, precipitation
724   acidity, and acid inputs to ecosystems. *Atmospheric Chemistry and Physics*, *20*(20), 12223–12245.
725   https://doi.org/10.5194/acp-20-12223-2020

726   Snider, G., Weagle, C. L., Murdymootoo, K. K., Ring, A., Ritchie, Y., Stone, E., et al. (2016). Variation in global
727   chemical composition of PM2.5: emerging results from SPARTAN. *Atmospheric Chemistry and Physics*, *16*(15),
728   9629–9653. https://doi.org/10.5194/acp-16-9629-2016

729   Sullivan, A. P., Guo, H., Schroder, J. C., Campuzano-Jost, P., Jimenez, J. L., Campos, T., et al. (2019). Biomass
730   Burning Markers and Residential Burning in the WINTER Aircraft Campaign. *Journal of Geophysical Research:*
731   *Atmospheres*, *124*(3), 1846–1861. https://doi.org/10.1029/2017JD028153

732   Sun, J., Zhang, Q., Canagaratna, M. R., Zhang, Y., Ng, N. L., Sun, Y., et al. (2012). Corrigendum to "Highly time-
733   and size-resolved characterization of submicron aerosol particles in Beijing using an Aerodyne Aerosol Mass
734   Spectrometer" [Atmos. Environ. 44 (2010) 131-140]. *Atmospheric Environment*, *47*(1), 570.

735   https://doi.org/10.1016/j.atmosenv.2010.01.023

736   Sun, Y. L., Zhang, Q., Schwab, J. J., Chen, W. N., Bae, M. S., Lin, Y. C., et al. (2011). A case study of aerosol
737   processing and evolution in summer in New York City. *Atmospheric Chemistry and Physics*, *11*(24), 12737–
738   12750. https://doi.org/10.5194/acp-11-12737-2011

739   Szopa, S., Balkanski, Y., Schulz, M., Bekki, S., Cugnet, D., Fortems-Cheiney, A., et al. (2013). Aerosol and ozone
740   changes as forcing for climate evolution between 1850 and 2100. *Climate Dynamics*, *40*(9–10), 2223–2250.
741   https://doi.org/10.1007/s00382-012-1408-y

742   Tian, P., Liu, D., Huang, M., Liu, Q., Zhao, D., Ran, L., et al. (2019). The evolution of an aerosol event observed from
743   aircraft in Beijing: An insight into regional pollution transport. *Atmospheric Environment*, *206*(July 2018), 11–
744   20. https://doi.org/10.1016/j.atmosenv.2019.02.005

745   Timonen, H., Aurela, M., Carbone, S., Saarnio, K., Saarikoski, S., Mäkelä, T., et al. (2010). High time-resolution
746   chemical characterization of the water-soluble fraction of ambient aerosols with PILS-TOC-IC and AMS.
747   *Atmospheric Measurement Techniques*, *3*(4), 1063–1074.

748   Twomey, S. (2007). Pollution and the Planetary Albedo. *Atmospheric Environment*, *41*(SUPPL.), 120–125.
749   https://doi.org/10.1016/j.atmosenv.2007.10.062

750   Wang, Q., Jacob, D. J., Spackman, J. R., Perring, A. E., Schwarz, J. P., Moteki, N., et al. (2014). Global budget and
751   radiative forcing of black carbon aerosol: Constraints from pole-to-pole (HIPPO) observations across the Pacific.
752   *Journal of Geophysical Research*, *119*(1), 195–206. https://doi.org/10.1002/2013JD020824

753   Wang, Y., Jacob, D. J., & Logan, J. A. (1998). Global simulation of tropospheric O3-NOx-hydrocarbon chemistry -
754   1. Model formulation. *Journal of Geophysical Research: Atmospheres*, *103*(3339), 10713–10725.
755   https://doi.org/10.1029/98jd00158

756   Weinheimer, A. J., Walega, J. G., Ridley, B. A., Sachse, G. W., Anderson, B. E., & Collins Jr, J. E. (1993).
757   Stratospheric NOy measurements on the NASA DC-8 during AASE II. *Geophysical Research Letters*, *20*(22),
758   2563–2566.

759   Weng, H., Lin, J., Martin, R., Millet, D. B., Jaeglé, L., Ridley, D., et al. (2020). Global high-resolution emissions of
760   soil NOx, sea salt aerosols, and biogenic volatile organic compounds. *Scientific Data*, *7*(1), 1–15.
761   https://doi.org/10.1038/s41597-020-0488-5

762   Van Der Werf, G. R., Randerson, J. T., Giglio, L., Van Leeuwen, T. T., Chen, Y., Rogers, B. M., et al. (2017). Global
763   fire emissions estimates during 1997-2016. *Earth System Science Data*, *9*(2), 697–720.
764   https://doi.org/10.5194/essd-9-697-2017

765   Westervelt, D. M., Pierce, J. R., Riipinen, I., Trivitayanurak, W., Hamed, A., Kulmala, M., et al. (2013). Formation
766   and growth of nucleated particles into cloud condensation nuclei: Model-measurement comparison.
767   *Atmospheric Chemistry and Physics*, *13*(15), 7645–7663. https://doi.org/10.5194/acp-13-7645-2013

768   Whitey, K. T. (1978). The physical characteristics of sulfur aerosols. In *Atmospheric Environment* (Vol. 41, pp. 25–
769   49). Elsevier. https://doi.org/10.1016/j.atmosenv.2007.10.057

770   Yu, F., & Luo, G. (2009). Simulation of particle size distribution with a global aerosol model: Contribution of
771   nucleation to aerosol and CCN number concentrations. *Atmospheric Chemistry and Physics*, *9*(20), 7691–7710.
772   https://doi.org/10.5194/acp-9-7691-2009

773   Zender, C. S., Bian, H., & Newman, D. (2003). Mineral Dust Entrainment and Deposition (DEAD) model: Description
774   and 1990s dust climatology. *Journal of Geophysical Research: Atmospheres*, *108*(14).
775   https://doi.org/10.1029/2002jd002775

776   Zhai, S., Jacob, D., Brewer, J., Li, K., Moch, J., Kim, J., et al. (2021). Interpretation of geostationary satellite aerosol
777   optical depth (AOD) over East Asia in relation to fine particulate matter (PM$_{2.5}$):
778   insights from the KORUS-AQ aircraft campaign and seasonality. *Atmospheric Chemistry and Physics*, 1–23.
779   https://doi.org/10.5194/acp-2021-413

780   Zhang, L., Kok, J. F., Henze, D. K., Li, Q., & Zhao, C. (2013). Improving simulations of fine dust surface
781   concentrations over the western United States by optimizing the particle size distribution. *Geophysical Research*

782   *Letters*, *40*(12), 3270–3275. https://doi.org/10.1002/grl.50591

783